

Statistical distribution of HI 21cm intervening absorbers as potential cosmic acceleration probes

Chang-Zhi Lu ^{1,2}, Tingting Zhang,³★ Tong-Jie Zhang ^{1,2,4} †

¹*Institute for Frontiers in Astronomy and Astrophysics, Beijing Normal University, Beijing 102206, China*

²*Department of Astronomy, Beijing Normal University, Beijing 100875, China*

³*College of Command and Control Engineering, PLA Army Engineering University, Nanjing 210017, China*

⁴*Institute for Astronomical Science, Dezhou University, Dezhou 253023, China*

Accepted 2023 March 10. Received 2023 March 10; in original form 2022 October 27

ABSTRACT

Damped Lyman- α Absorber (DLA), or HI 21cm Absorber (H21A), is an important probe to model-independently measure the acceleration of spectroscopic velocity (v_S) via the Sandage-Loeb (SL) effect. Confining by the shortage of DLAs and Background Radio Sources (BRSs) with adequate information, the detectable amount of DLAs is ambiguous in the bulk of previous work. After differing the acceleration of scale factor (\ddot{a}) from the first order time derivative of spectroscopic velocity (\dot{v}_S), we make a statistical investigation of the amount of potential DLAs in the most of this paper. Using Kernel Density Estimation (KDE) to depict general redshift distributions of BRSs, observed DLAs and a DLA detection rate with different limitations (1.4GHz flux, HI column density and spin temperature), we provide fitted multi-Gaussian expressions of the three components and their 1σ regions by bootstrap, with a proportional constant of H21As in detected DLAs, leading to the measurable number predictions of H21As for FAST, ASKAP and SKA1-Mid in HI absorption blind survey. In our most optimistic condition ($F_{1.4\text{GHz}} > 10\text{mJy}$, $N_{\text{HI}} > 2 \times 10^{20}\text{cm}^{-2}$ and $T_S > 500\text{K}$), the FAST, AKSAP and SKA1-Mid would probe about 80, 500 and 600 H21As respectively.

Key words: cosmology: dark energy – cosmology: observations – radio lines: galaxies – galaxies: ISM – methods: data analysis

1 INTRODUCTION

An accelerating expansion is happening in our Universe, whose acceleration has not been measured model-independently up to now. An unprecedentedly precise observational determination will provide more clues to the fundamental modeling of the expanding mechanism, such as the most recognized dark energy or many candidates of Equation of State.

Common cosmological probes offer the model-dependent acceleration of scale factor (\ddot{a}), while the first order time derivative of spectroscopic velocity (\dot{v}_S) of objects faithfully tracing the Hubble flow in real time are still beyond our reach. Proposed by Sandage (1962) and improved by Loeb (1998), the redshift drift, namely the Sandage-Loeb (SL) effect is a model-independent probe of \dot{v}_S and free of cosmic geometry, used to distinguish cosmological models (Codur & Marinoni 2021; Mishra 2022) and explore the inhomogeneity and anisotropy of the Universe (Buchert et al. 2022; Heinesen & Macpherson 2022). Moresco et al. (2022) recorded more details of redshift drift, and Melia (2022) discussed the significant differences between a zero and non-zero redshift drift universe.

Direct measurement of redshift drift mainly depends on Lyman- α forest (optical method) and Damped Lyman- α Absorbers (DLAs, ra-

dio method, our main concern in this paper). DLAs contain abundant dense HI gas (column density $N_{\text{HI}} > 2 \times 10^{20}\text{cm}^{-2}$) which absorbs Lyman- α photons (optical) and most 21cm radiation (radio) from radio sources in their local rest frame.

There are many studies about the physical properties of DLAs. Zwaan et al. (2005) analysed 355 HI 21cm line of nearby extragalaxies ($z \approx 0$) from Westerbork Synthesis Radio Telescope, showing that their physical properties and DLAs incident rate are aligned with those of high- z DLAs ($z > 2$) from quasar spectra. Prochaska & Wolfe (2009) researched HI column density distribution function in comoving redshift $f(N_{\text{HI}}, X)$ from a DLA survey in SDSS DR5, and argued that HI distribution barely evolves due to similar shapes of $f(N_{\text{HI}}, X)$ in redshift from 2.2 to 5.5. Using statistical sub-sample from BOSS (a part of SDSS-III) quasar spectra at $z > 2$, Noterdaeme et al. (2012) probed the N_{HI} distribution at $\langle z \rangle = 2.5$, and found it matches the observed opacity-corrected distribution well. Braun (2012) used opacity-corrected high-resolution images of local extragalaxies to generate $f(N_{\text{HI}}, X)$ at $z \approx 0$. The distributions f and the number of equivalent DLAs show systematic decreases compared with their high- z values. By defining a measurable covering factor (C_f), Kanekar et al. (2014) carefully studied the DLA's spin temperature (T_S) distribution in low and high redshift, within and beyond our galaxy, and the correlation between itself and N_{HI} , C_f and metallicity $[Z/H]$. Using quasar spectra from the Hubble Space Telescope archive, Neeleman et al. (2016) conducted the first DLA blind

★ E-mail: 101101964@seu.edu.cn(TTZ)

† E-mail: tjzhang@bnu.edu.cn(TJZ)

survey at $z < 1.6$ and analysed $f(N_{\text{HI}}, X)$ in a specific range of N_{HI} . Their DLA incidence was a bit lower but consistent with other results and uncertainties. [Rao et al. \(2017\)](#) used 70 MgII-preselected DLAs (with $z < 1.65$) to describe DLA number density in $0 < z < 5$ combining the $z=0$ modification and extra high- z DLAs. From SDSS-III DR12 DLAs data. [Bird et al. \(2017\)](#) revised $f(N_{\text{HI}}, X)$ and dN/dX , especially the latter at $z > 4$. Curran found that the reciprocal of T_S can trace the star formation density ψ^* ([Curran 2017b](#)), and the fraction of the cold neutral medium ($\int \tau dv / N_{\text{HI}}$) has relation to ψ^* ([Curran 2017a](#)). [Grasha et al. \(2020\)](#) evaluated $f(N_{\text{HI}}, X)$ per comoving redshift and per column density interval from detected absorptions and upper limits from non-detection regions. These works provided precious DLA samples and studied their multi-dimensional features, such as N_{HI} , T_S and $f(N_{\text{HI}}, X)$, which have been used in DLA amount predictions. Integrating both the linearly interpolated $f(N_{\text{HI}}, z)$ and the simulated completeness function $C(N_{\text{HI}}, T_S, v_{\text{FWHM}}, z)$ built from the FLASH early survey ([Allison et al. 2020](#)), they explored the posterior distribution of spin temperature ([Allison 2021](#)) considering different observations ([Sadler et al. 2020](#)), and the possible detection number ([Allison et al. 2022](#)) of intervening and associated HI 21cm absorbers given different constraints.

The first approach to \dot{v}_S , Lyman- α forests (LFs), was carefully investigated by [Liske et al. \(2008\)](#) for the next generation instrument ESO-ELT and was recently renewed by [Dong et al. \(2022\)](#). Optical Lyman- α absorbers are often discovered in intergalactic medium and likely have less peculiar acceleration ([Cooke 2020](#)). With abundant Lyman- α absorption in line forests, the LFs approach gathers much attention like the Cosmic Accelerometer project ([Eikenberry et al. 2019](#)), the ACCELERATION programme ([Cooke 2020](#)), ESPRESSO and NEID spectrographs ([Chakrabarti et al. 2022](#)). Interestingly, [Esteves et al. \(2021\)](#) concluded that measuring redshift drift and constraining cosmological parameters is a dilemma. However, confined by the earth's ionosphere, ground-based observations only receive LFs photons from $z \gtrsim 1.65$ ([Kloieckner et al. 2015](#)), which corresponds to the decelerating expansion and jerk era.

The second approach, HI 21cm Absorbers (H21As), which are usually discovered in DLAs, was first attempted practically by [Darling \(2012\)](#), in which they gave the best constraint (until now) on redshift drift of three magnitudes larger than theoretical prediction. Long-term frequency stability was verified in GBT and their used H21As. Not all DLAs (H21As) are suitable for \dot{v}_S observations. A common classification ([Curran et al. 2016](#)) divides DLAs into two types: associated (A-type, which are near the radio sources with statistically shallower and wider absorption profiles) and intervening (I-type, which are remote from the sources with deeper and narrower profiles), implying that I-type DLAs suffer less local effects and locate in colder and quieter regions, with fewer inner collisions and outside radiation. Therefore the I-type is more ideal for the observation of cosmic acceleration, and we abbreviate it as DLA hereafter. [Jiao et al. \(2020\)](#) made an HI 21cm absorption spectral observation in PARKES, advocating the necessity of consecutive (decade) high-resolution spectral observations against the high-velocity uncertainty. [Lu et al. \(2022\)](#) made a high-accuracy HI 21cm spectral observation with FAST as a preliminary effort to obtain a snapshot of the S-L signal, introducing semi-theoretical velocity uncertainties in one epoch. Further observations for stricter constraints are still applied and prepared.

The redshift number density of potential DLAs were produced by [Yu et al. \(2014, 2017\)](#) and [Jiao et al. \(2020\)](#), where they focused on CHIME, Tianlai and FAST respectively. [Zhang et al. \(2021\)](#) estimated the number of HI absorption lines from the radio luminosity function of radio-load AGNs. And recently [Allison et al. \(2022\)](#) eval-

uated it as mentioned before. The HI 21cm absorption surveys have found few new DLAs ([Dutta et al. 2017](#)), and the radio surveys obtained massive samples extended to deeper view and fainter sources ([Matthews et al. 2021](#)). Therefore it necessitates checking as many datasets to renew the redshift number density of BRSSs and DLAs. Meanwhile, many HI 21cm absorption survey programs are on schedule or undergoing, such as the First Large Absorption Survey in HI (FLASH) ([Allison et al. 2022](#)) in ASKAP telescope, MeerKAT Absorption Line Survey (MALS) ([Gupta et al. 2016, 2021](#)) in MeerKAT telescope, Widefield ASKAP L-band Legacy All-sky Blind survey (WALLABY) ([Koribalski et al. 2020](#)) in ASKAP too, will flesh our understanding of 21cm DLAs. Any advance in these aspects would modify the final anticipation of cosmic acceleration experiments in the radio approach.

In this paper, the difference in definition between the measured spectral acceleration (\dot{v}_S) and the real cosmic (scale factor) acceleration (\ddot{a}) is stressed again in sec 2. With KDE to depict data and bootstrap to give the 1σ errors, we study the redshift number density of Background Radio Sources (BRSSs) in sec 3.1 and observed DLAs in sec 3.2 where we also explore DLA detection rate function and the fraction of H21As to DLAs, and estimate the detectable amount of potential H21As for FAST, ASKAP and SKA1-Mid in sec 3.3. Our discussion and conclusion are in sec 4 and 5. All the calculation in this paper is based on a fiducial Planck18 Λ CDM model ($\Omega_{\text{K}0} = \Omega_{\text{R}0} = 0$, $\Omega_{\text{M}0} = 0.315$, $H_0 = 67.4 \text{ km s}^{-1} \text{ Mpc}^{-1}$) ([Planck Collaboration 2020](#)).

2 COSMIC ACCELERATION

For many papers containing the necessary formulae and derivations such as [Liske et al. \(2008\)](#), we give a brief description with a standard Λ CDM model.

The expansion rate in Λ CDM is:

$$E(z) = \sqrt{\Omega_{\text{R}0}(1+z)^4 + \Omega_{\text{M}0}(1+z)^3 + \Omega_{\text{K}0}(1+z)^2 + \Omega_{\Lambda 0}}, \quad (1)$$

where z is redshift, and $\Omega_{\text{R}0}$, $\Omega_{\text{M}0}$, $\Omega_{\text{K}0}$, $\Omega_{\Lambda 0}$ are today's density parameters of radiation, matter, curvature and dark energy respectively. The redshift drift of Hubble-flow tracers is:

$$\Delta z \approx \frac{\dot{a}_0 - \dot{a}(z)}{a(z)} \Delta t_0 = H_0 [1 + z - E(z)] \Delta t_0, \quad (2)$$

where $t_0 = t_{\text{obs}}$ is the time of observer, $a_0 = a(t_0)$ is today scale factor, the dot in a represents the derivative with respect to t_0 , and H_0 is Hubble constant.

The change of its spectroscopic radial velocity ($v_S = cz$) is:

$$\Delta v_S \approx \frac{c}{1+z} \Delta z \approx c [\dot{a}_0 - \dot{a}(z)] \Delta t_0 = c H_0 \left[1 - \frac{E(z)}{1+z}\right] \Delta t_0. \quad (3)$$

The velocity drift is an indicator of \dot{a} differences ($\dot{a}_0 - \dot{a}(z)$). And according to eq. 3, we can use measured \dot{v}_S to further infer $\Delta \dot{a}$ and \ddot{a} model-independently.

When we explain the cosmic expansion with general relativity (GR), the recession velocity is ([Davis & Lineweaver 2001](#)):

$$v_G = \dot{a}(z) D_C(z) = \frac{c}{H_0} \dot{a}(z) \int_0^z \frac{dz'}{E(z')}, \quad (4)$$

where $D_C(z) = c \int_0^z \frac{dz'}{H(z')}$ is the comoving distance. The first order time derivative of v_G is ([Jiao et al. 2020](#)):

$$\dot{v}_G = \ddot{a}(z) D_C(z) + \dot{a}(z) \dot{D}_C(z) = \ddot{a}(z) D_C(z) + \dot{a}(z) \frac{dD_C(z)}{dz} \frac{dz}{dt_0}. \quad (5)$$

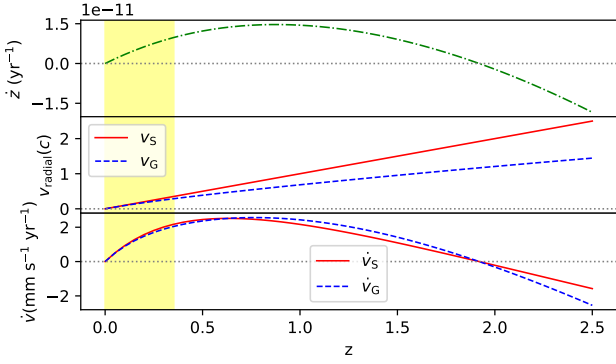


Figure 1. Several physical quantities versus redshift. In the upper panel, the green dashed-dotted line is the redshift drift (eq. 2). In the middle panel, the red solid and blue dashed lines are the spectroscopic radial and GR recession velocities (eq. 4). In the bottom panel, we show their corresponding velocity drifts (eq. 3 and 5). The pale yellow block across three panels covers the redshift range of FAST (0 \sim 0.352) (Li et al. 2018).

In order to conveniently plot \dot{v}_G , from the expression of deceleration parameter $q(z)$, we could write down $\ddot{a}(z)$:

$$q(z) = \frac{1+z}{2E^2(z)} \frac{dE^2(z)}{dz} - 1, \quad (6)$$

$$\ddot{a}(z) = -H_0^2 q(z) a(z) E^2(z). \quad (7)$$

Only \ddot{a} can depict the physical process of deceleration or acceleration of the universe expansion, and have a consistent value at any point from any distance in the same moment, for the scale factor is generalized to the whole universe.

The observed \dot{z} (or \dot{v}_S) involves a comparison within a pair of space-time spots (today-observer and past-source). For a fixed source, its \dot{z} (or \dot{v}_S) would change with the observer's position selection. Thus it is just a relative measurement of the apparent velocity changes for a specific local observer. Although we do measure it, it does not represent the real acceleration of the Universe's expansion. Moreover, through a secular (decade) observation, we can derive a time-averaged \dot{a} drift ($\overline{\Delta\dot{a}}$) from Δv_S in eq. 3.

From Figure 1, the zero-points of \ddot{a} and \dot{z} (or low-redshift approximated \dot{v}_S) are very different, where the former ($z_{a0} \approx 0.6$) relies on $q(z)$ and the latter ($z_{z0} \approx 1.9$) depends on $1+z-E(z)$.

From the upper panel in Figure 2, the universe expands in acceleration at $z < z_{a0}$ ($\ddot{a} > 0$), and the universe expands in deceleration at $z > z_{a0}$ ($\ddot{a} < 0$). But z_{z0} cannot distinguish between the two states. For example, when $z < z_{z0}$, the observed $\dot{v}_S \propto (\dot{a}_0 - \dot{a}_z)$ is always positive, but it does not mean the whole universe expanding acceleratingly from z_{z0} to $z = 0$. Instead, it only proves that the observed point is escaping us visually during this era.

From the lowest panel in Figure 2, if our Universe is genuinely dominated by a Λ CDM model, we could safely research spectroscopic acceleration (\dot{v}) with good approximation at $z \lesssim 2$.

After distinguishing \dot{v}_S and \ddot{a} , in the following sections, we use existing radio sources and H21As samples to make a realistic number prediction, for the purpose that one can observe them to better constrain \dot{v}_S via the radio approach.

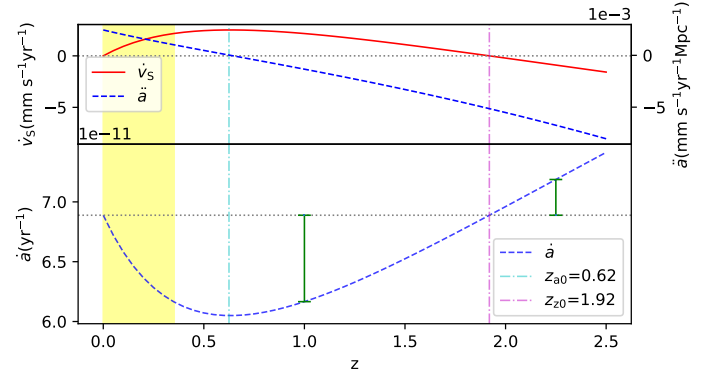


Figure 2. The measurable \dot{v}_S and theoretical \ddot{a} . The upper panel contains \ddot{a} (the blue dashed line, eq. 7) and \dot{v}_S (the red line, eq. 3). In the lower panel, the blue dashed line is $\dot{a} = a(z)H(z)$. The left vertical cyan dashed-dotted line is the zero-point of \ddot{a} , while the right vertical magenta dashed-dotted line is the zero-point of \dot{z} (or \dot{v}_S). We use two short green bars to emphasise the positive or negative value of $\dot{v}_S \propto (\dot{a}_0 - \dot{a}_z)$. The pale yellow block is the FAST redshift coverage.

3 EXPECTATION OF HI 21CM ABSORPTION SYSTEMS

The redshift number density of potential H21As in every square degree of the sky with three lowest detection limitations, i.e. flux density (F) of BRSs, HI column density (N_{HI}) and spin temperature (T_S) of DLAs, could be expressed as

$$n_{21S}(z, F, N_{\text{HI}}, T_S) = \eta_{21}(z) \int_{N_{\text{HI}}}^{\infty} \int_{T_S}^{\infty} \kappa(z, N', T') n_{\text{D}}(z, N') dN' dT' \times \int_F^{\infty} \int_z^{\infty} n_{\text{R}}[z' + \Delta Z(z'), F'] dz' dF'. \quad (8)$$

$n_{\text{R}}(z, F)$ is the number density of BRS per square degree related with redshift z and observed 1.4GHz flux density F . $n_{\text{D}}(z, N_{\text{HI}})$ is the number density of observed DLAs in every possible sightline directing toward a BRS with z and HI column density N_{HI} . $\kappa(z, N_{\text{HI}}, T_S)$ is the DLA detection rate at a given N_{HI} and T_S level. $\eta(z)$ is the proportion of H21As in DLAs with z . Moreover, $\Delta Z(z)$, used in Allison (2021), excludes the background galaxy near its foreground DLA within the radial velocity of 3000km/s:

$$\Delta Z(z) = 3000(1+z)/c, \quad (9)$$

where c is the speed of light.

3.1 Prediction of BRSs

The common redshift distribution of radio sources in predicting potential-DLA detectable number is (de Zotti et al. 2010):

$$n_{\text{R}}(z) = 1.29 + 32.37z - 32.89z^2 + 11.13z^3 - 1.25z^4, \quad (10)$$

which came from a z -binned polynomial fitting of the CENSORS data (Brookes et al. 2008). However, the polynomial will be negative when z exceeds 3.5. Besides, the expression contains radio sources with $F_{1.4\text{GHz}} \leq 10\text{mJy}$, which are faint and time-expensive in a blind survey to acquire prominent absorption lines.

The Combined EIS-NVSS Survey of Radio Sources (CENSORS) targeted the ESO Imaging Survey (EIS) Patch D, covering a $3 \times 2\text{deg}^2$ field of view and 150 sources preselected from NRAO VLA Sky

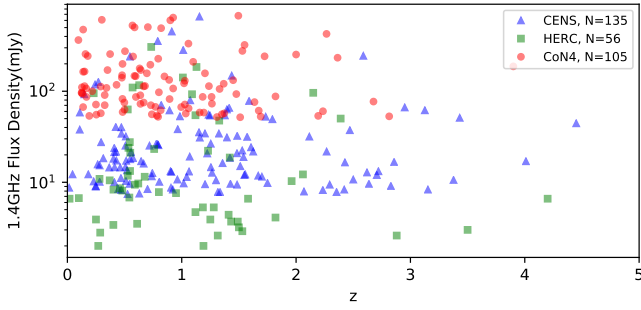


Figure 3. The distribution of three radio datasets. The blue triangles, green squares and red circles from CENSORS, Hercules and CoNFIG-4 respectively, are our used sources. Their amounts are listed in the legend.

Survey (NVSS) (Condon et al. 1998). Rigby et al. (2011) presented a 135-sample subset of CENSORS at a $F_{1.4\text{GHz}}$ completeness of 7.2mJy. The extra $F_{1.4\text{GHz}}$ can provide more information and limitation in the BRS distribution.

Besides, Marcos-Caballero et al. (2013) made a z -binned gamma fitting for CENSORS. When comparing the galaxy angular power spectrum via the Bayesian evidence test, the gamma fitting outperformed the polynomial one.

3.1.1 More Datasets

The CENSORS provides many samples for radio-source redshift resolution. Nonetheless, can the $n_R(z)$ from a 6deg^2 survey represent the whole sky situation? Considering the varied physical conditions toward every sky direction in every matter cluster, it still deserves verification with more radio datasets. The LBDS-Hercules (Waddington et al. 2001) and CoNFIG-4 (Gendre et al. 2010) covering the different sky areas are satisfied.

The Leiden-Berkeley Deep Survey (LBDS) Hercules has 64 radio sources with $F_{1.4\text{GHz}} > 2\text{mJy}$ in a 2deg^2 sky, and we use the data collected by Rigby et al. (2011). The Combined NVSS-FIRST Galaxies-4 (CoNFIG-4) contains 184 radio sources with $F_{1.4\text{GHz}} > 50\text{mJy}$ in a 52deg^2 sky. The additional two sets greatly improve our analysis.

Firstly our radio datasets were made ten years ago, so we update them following the NVSS catalogue. New sources belonging to the sky coverage of CoNFIG-4 are listed in Table 1.

Then we plot the distributions of all BRSs with $z \geq 0.1$ (beyond the local supercluster, but including a sample of $z=0.0963$ from CoNFIG-4) in Figure 3, and list the count of different 1.4GHz flux levels in Table 2. The flux counts are quite imbalanced between the CENSORS and Hercules, indicating a possible sky coverage bias.

To keep samples rich enough, we use CENSORS and Hercules to estimate the BRS z probability density with $F_{1.4\text{GHz}} \geq 10\text{mJy}$ and all sets to the z density with $F_{1.4\text{GHz}} \geq 50\text{mJy}$.

Although our CoNFIG-4 dataset contains the original 184 and extra 3 extra radio sources, only 105 of them have $z \geq 0.0963$. Therefore we re-scale the sky coverage as $105/187 * 52 \approx 29.2\text{deg}^2$, to counteract the lost z information.

3.1.2 New Descriptions and One Example

Polynomial fitting often has intractable zero points. Specific fitting models such as gamma require more prior knowledge. And different-length z -bin would lose diverse information in the process.

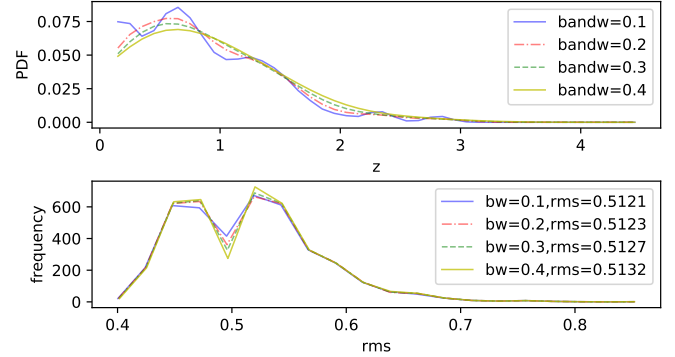


Figure 4. The different bandwidths in CoNFIG-4 KDE. In the upper panel, the blue, red dashed-dotted, green dashed and yellow solid curves are the PDF with bandwidths from 0.1 to 0.4. In the lower panel, four curves are the rms error distribution in 500 rounds' cross-validation, their colors correspond to the upper, and their mean rms are shown in the legend.

Consequently, we introduce the Kernel Density Estimation (KDE) to implement a non-parametric fitting of z probability density without bins. Particularly when using a Gaussian kernel, the final distribution can be extracted by multi-Gaussian fitting. In the next paragraphs, we will show the data process of CoNFIG-4 with $F_{1.4\text{GHz}} \geq 50\text{mJy}$ as an example. For other datasets following the same procedure, we would give results directly.

The scale of abscissa would affect the profile's height, so we fix the gap of z as 0.1 at the start.

We use Gaussian kernel KDE (*KernelDensity* in sklearn) to fit the CoNFIG-4 data (both z and $F_{1.4\text{GHz}}$). KDE has a key parameter 'bandwidth' equivalently controlling the width of a single Gaussian count unit, which replaces a single rectangle count unit in a histogram. Narrower bandwidth remains more features, but leads to a more flexible model and less generalization capability.

For instance, we plot the fitted Probability Density Function (PDF) with several bandwidths in the upper panel of Figure 4 and show their rms error count from 500 rounds' 8-fold random-shuffle cross-validation in its lower panel. The mean rms error decreases when the bandwidth diminishes, and the rms error distribution keeps stable. However, the 0.1-bandwidth at least needs a 5-Gaussian profile to fit. Thus we accept a bandwidth ≥ 0.2 but as small as possible and always prefer a simpler multi-Gaussian fitting.

Next, we explore what statistical model covers CoNFIG-4 better. Noticing the denser low-redshift region, we use exponential, gamma and Weibull distribution to fit the data.

We use Kolmogorov-Smirnov(K-S) test (*kstest* in scipy) to compare their fittings. If it returns a p-value higher than our expected level of significance ($\alpha = 0.05$), we can regard the two arrays from the same distribution. It shows the p-values 0.0815 of the norm and 0.0573 of exponential (exp), while gamma and Weibull both have p-values lower than 0.05. But the auto K-S test can not process the KDE curve. Therefore in manual coding, we plot the Cumulative Distribution Function (CDF) of real 0.1- z -bin data, exponential, KDE curve of bandwidth 0.2 and 0.3 in Figure 5, and compare the maximum Vertical Distances (maxVDs) between real data CDF and tested CDF. Now we define a constant:

$$C(\alpha, m, n) = \sqrt{-\frac{1}{2} \ln\left(\frac{\alpha}{2}\right)} \sqrt{\frac{m+n}{m*n}}, \quad (11)$$

where α is the significant level, m and n are the numbers of real samples and tested samples. We gain the KDE profile from real

Table 1. Additional radio sources in the sky coverage of CoNFIG-4

Source Name	RA Dec(J2000) (h:m:s d:m:s)	z	$F_{1.4\text{GHz}}$ (mJy)	Reference ¹
QSO J1407-0049	14 07 10.59 -00 49 15.3	1.51117	51.8	[A09]
SDSS J143031.30-000907.5 ²	14 30 31.45 -00 09 08.0	2.8143	53	[A15]
NVSS J143403+010351 ²	14 34 03.22 +01 03 51.5	1.06	64.9	[T19]
TXS 1423+019 ²	14 26 30.42 +01 42 36.1	0.3263	90.8	[G19]
TXS 1408+016 ²	14 11 08.29 +01 24 41.1	3.9	187.5	[M19]
TXS 1420+018 ²	14 23 03.43 +01 39 58.7	1.1	210.4	[M19]
LBQS 1438+0210	14 40 59.50 +01 57 43.9	0.7944	227.6	[A15]
NVSS J140639-032430	14 40 59.50 +01 57 43.9	2	253	[X14]
TXS 1434-003 ²	14 37 21.09 -00 33 18.1	0.0963	365.0	[M19]
TXS 1406+015 ²	14 08 33.31 +01 16 22.1	0.9	601.3	[S06]

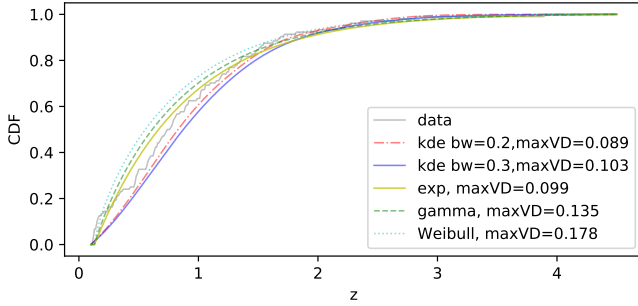
¹ [A09](Abazajian et al. 2009), [A15](Alam et al. 2015), [T19](Toba et al. 2019), [G19](Garon et al. 2019), [M19](Ma et al. 2019), [X14](Xu & Han 2014), [S06](Schmidt et al. 2006).

² These radio sources were originally contained in CoNFIG-4 dataset but without z information.

Table 2. 1.4GHz flux counts of datasets with $z \geq 0.1$

dataset	$N(F_{1.4\text{GHz}} \geq 50\text{mJy})$	$N(F_{1.4\text{GHz}} \geq 10\text{mJy})$	$N(\text{all})$
CENSORS	25	108	135
Hercules	11	25	56
CoNFIG-4	105	105	105 ¹

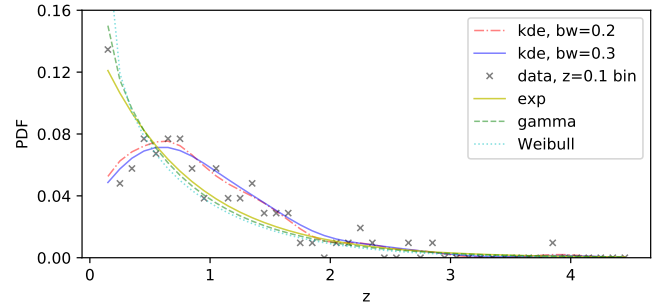
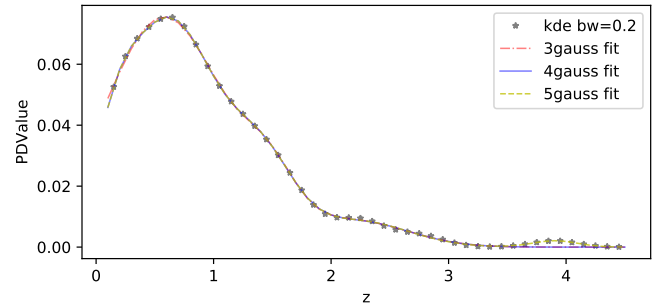
¹ CoNFIG-4 data include a sample of $z=0.0963$.


Figure 5. The CDF for manual K-S test. The gray, red dashed-dotted, blue, yellow, green dashed and cyan dotted curves are the CDFs of real data(CoNFIG-4), 2 KDEs($bw=0.2, 0.3$), exp, gamma and Weibull respectively. Their maxVDs are listed in the legend.

samples, so $C(0.05, 104, 104) \approx 0.1883$. If maxVD is less than the constant C, we can treat the two arrays from the same distribution.

From Figure 5, the exp and 2 KDEs comparatively fit real data from the aspect of maxVD. We plot their PDFs in Figure 6, where the exp and 2 KDEs are distinct. The gamma and Weibull are worse than the exp because their p-values are lower than 0.05. Though the exp matches the peak point well, it behaves poorly at the adjacent redshifts, causing the overestimation in our most concerned low-redshift ($z < 1$) region.

Finally, multi-Gaussian fitting exports an analytic expression for the BRS integration in eq. 8. To balance the informative feature and simple model, we plot the 0.2-bandwidth fitting in Figure 7 and choose the 3-Gaussian result.


Figure 6. The fitted PDF of CoNFIG-4. The gray cross is the Probability Density Law(PDL) of the real data. The red dashed-dotted, blue, yellow, green dashed and cyan dotted curves are the PDFs of 2 KDEs ($bw=0.2, 0.3$), exp, gamma and Weibull separately.

Figure 7. The multi-Gaussian fitting of KDE with bandwidth 0.2 for CoNFIG-4. The gray star is KDE data. The red dashed-dotted, blue and yellow dashed curves are 3-, 4- and 5-Gaussian models separately.

Because we mainly concern with the KDE performance, we will ignore other statistical model fittings hereafter.

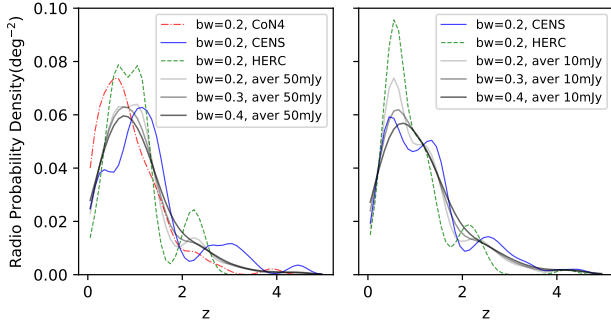


Figure 8. The multi-Gaussian fitting of the KDE curve with bandwidth 0.2 for all radio datasets. The left panel is for $F_{1.4\text{GHz}} \geq 50\text{mJy}$ and the right is for $F_{1.4\text{GHz}} \geq 10\text{mJy}$. The red dashed-dotted, blue and green dashed curves are the 0.2-bandwidth KDE results of CoNFIG-4, CENSORS and Hercules separately. The gray lines are the number-weighted KDEs with different-bandwidth components.

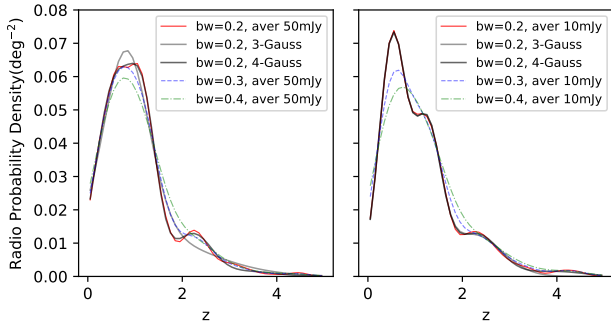


Figure 9. The multi-Gaussian fitting of averaged 0.2-bandwidth radio KDE curve. The left panel is for $F_{1.4\text{GHz}} \geq 50\text{mJy}$ and the right is for $F_{1.4\text{GHz}} \geq 10\text{mJy}$. The red, gray and black curves are the KDE averaged result and its KDE (bandwidth=0.2, 0.3) individually. The blue dashed and green dashed-dotted lines are the averaged other-bandwidth radio KDE.

3.1.3 Probability Density of BRSS

According to the H21A spectroscopic observation (Geréb et al. 2015), where 3 BRSS in all 32 ones showed $F_{1.4\text{GHz}} \leq 50\text{mJy}$ (but $\geq 35\text{mJy}$). Thus 50mJy can be a proper lower limit for the present observation capability. And we regard 10mJy as an optimistic capability for the next generation of radio telescopes or arrays.

We make KDE for different radio sets, accumulate with two flux levels (50mJy and 10mJy), check with manual K-S test, average them with the weights of their number density per square degree sky ($\sigma_{\text{CO}50} = 3.5962$, $\sigma_{\text{CE}50} = 4.1667$, $\sigma_{\text{HE}50} = 5.5$, $\sigma_{\text{CE}10} = 18$, $\sigma_{\text{HE}10} = 12.5$), and plot these in Figure 8, where larger bandwidths relate to simpler models, but lose more features, especially merging the first two peaks, which heavily impact our estimation in the low- z region. Therefore, we fix the bandwidth as 0.2.

We make multi-Gaussian fitting for a 2-dimension ($z-F_{1.4\text{GHz}}$) 0.2-bandwidth KDE curves in Figure 9. The 3-Gaussian is our prioritized option for simplicity. But in the high- z region ($z > 4$) of the 10mJy lower limit, it loses the last peak and causes an irreparable decrease compared with the 50mJy lower limit, even considering the 2 area number densities. Such inconsistency obliges us to add an extra Gaussian component to solve it, and the final 4-Gaussian fitting parameters and their 1σ errors are given in Table 3.

Table 3. Multi-Gaussian fitting of averaged 0.2-bandwidth radio KDE curves

component	a^1	μ^1	σ^1
50mJy-1	0.0579 ± 0.0011	0.5790 ± 0.0187	0.3930 ± 0.0123
50mJy-2	0.0395 ± 0.0030	1.1939 ± 0.0111	0.2711 ± 0.0084
50mJy-3	0.0124 ± 0.0002	2.2123 ± 0.0168	0.4869 ± 0.0208
50mJy-4	0.0012 ± 0.0002	4.0000 ± 0.1029	0.5000 ± 0.1178
10mJy-1	0.0706 ± 0.0003	0.5193 ± 0.0023	0.2788 ± 0.0016
10mJy-2	0.0447 ± 0.0003	1.2491 ± 0.0033	0.3031 ± 0.0042
10mJy-3	0.0127 ± 0.0001	2.2949 ± 0.0122	0.5049 ± 0.0147
10mJy-4	0.0015 ± 0.0001	4.0488 ± 0.0515	0.5000 ± 0.0588

¹ Gaussian function is $f(z) = \frac{a}{\sqrt{2\pi}\sigma} \exp\left[-\frac{(z-\mu)^2}{2\sigma^2}\right]$.

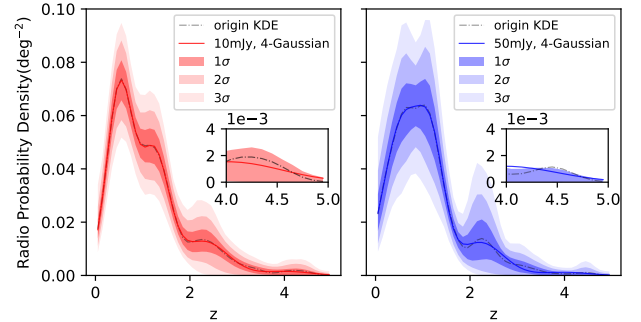


Figure 10. The PDF and 3σ errors of 0.2-bandwidth radio KDE curve. The left panel is for $F_{1.4\text{GHz}} \geq 50\text{mJy}$ and the right is for $F_{1.4\text{GHz}} \geq 10\text{mJy}$. The solid and dashed-dotted lines are 4-Gaussian fitted and their original KDE curve. The darkest and lightest areas are the 1σ and 3σ errors respectively. The inserted small panels zoom in their own tails in the high- z region, showing the imperfection of the fourth component.

The fourth Gaussian in 2 KDEs are constrained insufficiently: the a , μ and σ approach their set borders of 0.15 ($a+$), $4(\mu-)$ and 0.5 ($\sigma+$). If we loosen the borders, the 4-Gaussian tends to become the 3-Gaussian again. Actually, our intention is to derive an approximate KDE expression for numerical integration, and the 4-Gaussian fitting traces the KDE better than the 3-Gaussian, which is enough. Besides, we find that the former 3 components (8 parameters, excluding σ_3) are insensitive to the slight change of limitation (keeping $\mu_4 > 3.5$), varying less than 5% (σ_3 is 20%) and 10% in the fitted values and errors. Moreover, the curve tails ($z > 4$) are quite small, only covering less than 1% of the total area under the curve. Therefore we choose to use the 4-Gaussian.

The errors in Table 3 come from our used samples, and do not reflect the uncertainty including sampling, which need the bootstrap method to convey. The bootstrap randomly re-samples from the original dataset (A_0) with replacement forming a number of new datasets ($\mathcal{A}_N = \{A_i\}_N$, often $N \geq 1000$) with the same data volume. One conducts statistical inference from the newly generated sets (\mathcal{A}_N) assuming the A_0 and \mathcal{A}_N from the almost same underlying population. Thus, it provides a more robust 1σ estimation from the potential sample variations, particularly for small sample data.

We re-sample the three radio datasets 10000 times separately, make number-weighted 0.2-bandwidth KDE, extract its 3σ range in every abscissa (z) point, and plot them in Figure 10. The bootstrap 1σ errors are more inclusive than the parameter-fluctuation errors in multi-Gaussian (Table 3), and used by us.

The above procedure gives the radio source z probability den-

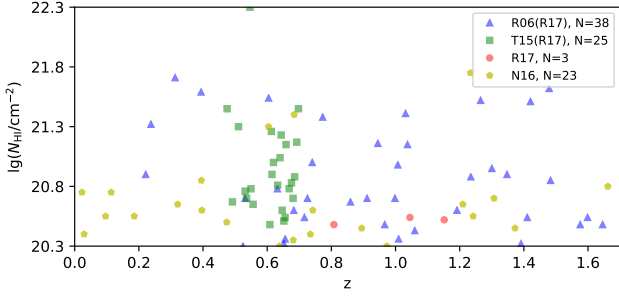


Figure 11. The distribution of 87 DLAs for number density n_D . The blue triangles, green squares and red circles from R06, T15 and R17 separately. The three datasets were all included in R17 article. The yellow pentagons come from N16. Their sample amounts are listed in the legend.

sity with different $F_{1.4\text{GHz}}$ levels, which needs to multiply with a number density per square degree sky σ to become number density. With number-weighted average from the three datasets, we obtain $\sigma_{50} = (105^2/29.2 + 25^2/6 + 11^2/2)/(105 + 25 + 11) \approx 3.714$ and σ_{10} is 16.966. Similar to Allison et al. (2022), we also search the σ in the whole NVSS catalogue with a max radio diameter filter ($\theta < 60\text{arcsec}$) to exclude the extended BRSSs, which worsens the covering factor of DLA. Given that the NVSS covers 82% of the entire sky (33830 deg^2), we collect $N_{50\text{mJy}}=125525$ and $N_{10\text{mJy}}=544130$, finally adopting $\sigma_{50}=3.71$ and $\sigma_{10}=16.09$ instead of σ_{50} and σ_{10} .

3.2 Forecasting of observed H21As

The recent research of DLA distribution at wide z region ($0 \lesssim z \lesssim 5$) was advanced by Rao et al. (2017). They provided an optical MgII preselection criterion of DLAs, used it to identify 70 DLAs at low z region ($z \lesssim 1.65$) from 369 MgII absorbers, and combined many high- z ($z \gtrsim 1.65$) SDSS-detected DLAs and a low- z modified value to give a global redshift number density:

$$n_{D\text{glo}}(z) = (0.027 \pm 0.007)(1+z)^{(1.682 \pm 0.200)}. \quad (12)$$

Although their result is enough for the z evolution of DLAs, they smoothed out the local DLA distribution features by three wide z bins, which is inadequate for cosmic acceleration observation. So we use their identified 64 DLAs ($N_{\text{HI}} > 2 \times 10^{20} \text{ cm}^{-2}$) from 369 MgII absorbers, and miss 6 DLAs from their full samples. First, Rao et al. (2006) presented 41 DLAs from 197 MgII absorbers, while we only find 38 DLAs with $W_0^{\lambda 2796} > 0.6$. Then, Turnshek et al. (2015) selected 26 DLAs from 96 MgII absorbers, while we just extract 23 DLAs. Neeleman et al. (2016) provided extra 23 DLAs with z and N_{HI} . We plot all 87 DLAs in Figure 11.

Similarly, we make 2-dimension (z - N_{HI}) KDE for the 87 DLAs with two lower N_{HI} levels, $N_{\text{HI}} > 2 \times 10^{20} \text{ cm}^{-2}$ ($\lg N_{\text{HI}} > 20.3$ for visual simplicity, although it should be $\lg(N_{\text{HI}}/\text{cm}^{-2}) > 20.3$) and $N_{\text{HI}} > 6.31 \times 10^{20} \text{ cm}^{-2}$ ($\lg N_{\text{HI}} > 20.8$), and use manual K-S test to compare the constant C and their maxVDs. Provided the simple profiles of KDE in Figure 12, we choose a 3-Gaussian fitting with 0.1 bandwidth for accuracy, and list the fitted values and errors in Table 4. A 10000-bootstrap gives the 1σ errors in Figure 13.

With the 21cm absorption optical depth $\tau_{21}(\nu) = -\log\{1 - \Delta F(\nu)/[C_f F(\nu)]\}$, N_{HI} can be expressed as (Kanekar et al. 2014):

$$N_{\text{HI}} = 1.823 \times 10^{18} T_S \int -\log\left[1 - \frac{\Delta F(\nu)}{C_f F(\nu)}\right] d\nu, \quad (13)$$

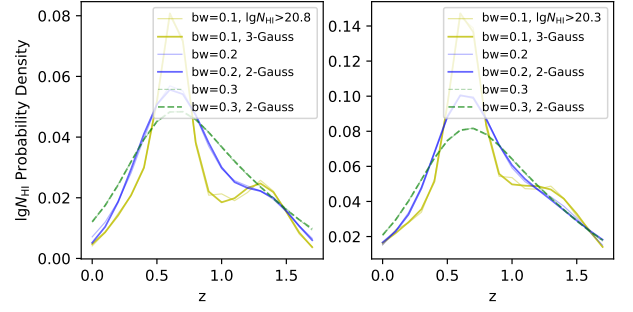


Figure 12. The multi-Gaussian fittings of KDE curves for 87 DLAs with different bandwidths. The left panel is for $\lg N_{\text{HI}} \geq 20.8$ and the right is for $\lg N_{\text{HI}} \geq 20.3$. The thin pale curves are KDE curves with different bandwidths, and the thick dark lines are their fittings respectively.

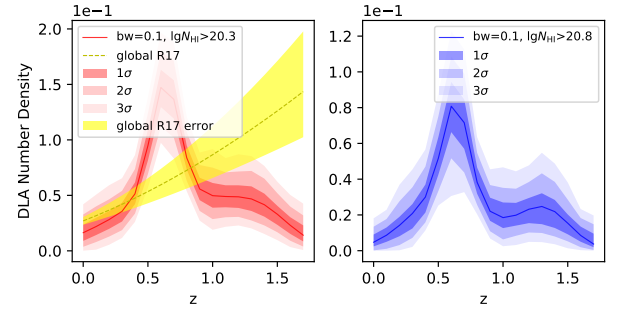


Figure 13. The number distribution and 3σ errors of 87 DLAs. The left panel is for $\lg N_{\text{HI}} \geq 20.3$ and the right is for $\lg N_{\text{HI}} \geq 20.8$. The solid lines are their 3-Gauss fitting of KDE curves, and the colored areas present the 3σ regions individually. The yellow dashed line and area in the left panel are the DLA number distribution and error region from R17.

Table 4. Multi-Gaussian fitting of 0.1-bandwidth DLA KDE curves

component	a	μ	σ
20.8-1	0.0323 \pm 0.0016	0.5789 \pm 0.0097	0.2953 \pm 0.0098
20.8-2	0.0517 \pm 0.0015	0.6350 \pm 0.0020	0.0993 \pm 0.0028
20.8-3	0.0231 \pm 0.0006	1.3149 \pm 0.0084	0.2007 \pm 0.0077
20.3-1	0.1025 \pm 0.0021	0.6336 \pm 0.0018	0.1099 \pm 0.0024
20.3-2	0.0509 \pm 0.0024	0.7506 \pm 0.0495	0.4782 \pm 0.0388
20.3-3	0.0233 \pm 0.0059	1.3649 \pm 0.0197	0.2273 \pm 0.0315

where T_S and C_f is spin temperature and covering factor of DLA, ΔF is the absorbed flux density, and F is the continuum flux density. Because of the low 21cm optical depth ($\tau_{21} \ll 1$) for most DLAs, eq. 13 can reduce to:

$$N_{\text{HI}} = 1.823 \times 10^{18} \frac{T_S}{C_f} \int \frac{\Delta F(\nu)}{F(\nu)} d\nu. \quad (14)$$

N_{HI} is determined by T_S , C_f and integrated percent absorption. Constraints on N_{HI} can be decomposed into three parts.

However, according to the same article (Kanekar et al. 2014), no statistical relations are found in T_S - N_{HI} and T_S - C_f , while $N_{\text{HI}} - \int \tau_{21}(\nu) d\nu$ has a 3.8σ -significance correlation. They find a 37-DLA dataset with their z , N_{HI} , estimated T_S and C_f in the foreground of compact radio quasars. Depending on this dataset, we will make a

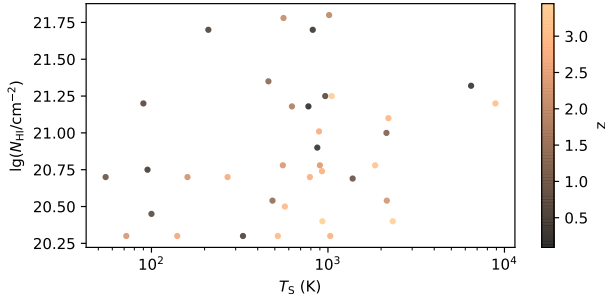


Figure 14. The distribution of 37 DLAs for detection rate κ . The darker sample has a larger redshift.

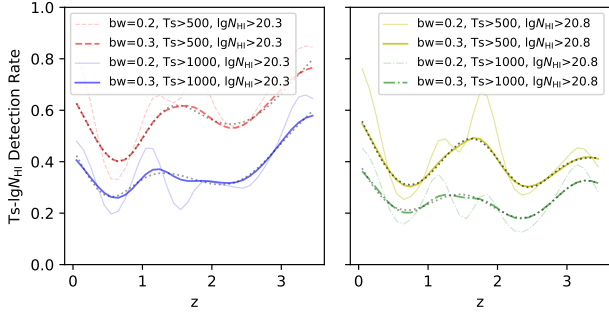


Figure 15. The multi-Gaussian fittings of KDE curves for 37 DLAs with different bandwidths. The left panel is for $\lg N_{\text{HI}} \geq 20.3$ and the right is for $\lg N_{\text{HI}} \geq 20.8$. The thin pale curves are 0.2-bandwidth KDE curves and the thick dark lines are 0.3-bandwidth ones. The unlabeled gray dotted lines are 3-Gaussian fitting for 0.3-bandwidth KDEs.

3-dimension KDE in the parameter space of z - N_{HI} - T_S , and limit N_{HI} and T_S as before. Because the N_{HI} - C_f relation was not explored in their paper, we do not limit C_f together.

Grasha et al. (2020) found the best T_S is $175/C_f$ K for low- z ($z < 1$) DLAs, and $100/C_f$ - $500/C_f$ K is acceptable. Allison (2021) obtained 274K and 576K in the low- z region ($z < 1$) in the detection and non-detection situations (2σ). Overall, we take T_S of 500K and 1000K as two limits, with the former two $\lg N_{\text{HI}}$ limits (20.3, 20.8) in our estimation of $\kappa(z, \lg N_{\text{HI}}, T_S)$.

Again, we plot the extra 37 DLAs in Figure 14. Making 3-dimension KDE with T_S and $\lg N_{\text{HI}}$ limits and conducting a manual K-S test, we perform a 3-Gaussian fitting (considering the actual shape of detection rate curves, we use one subtract the 3-Gaussian as the results) with 0.3 bandwidth in Figure 15 with their parameters listed in Table 5. The less bandwidth and more Gaussians are discarded to alleviate overfitting. The 3σ errors from 10000-bootstrap are offered in Figure 16. The 20.3-500 situation in Table 5 has the most unsuccessful constraint, reflected by the widest 3σ region in Figure 16. But considering the good performance between the KDE curve and its multi-Gaussian fitting, we still accept the results.

3.3 Anticipation of potential H21As

Given all the components, we can calculate the potential H21As number density (eq. 8) in Figure 17 and its integrated number count in Figure 18 from $z=0.1$ to eliminate the objects in the local Universe.

FAST covers about 24000deg^2 (Li et al. 2018) and the redshift

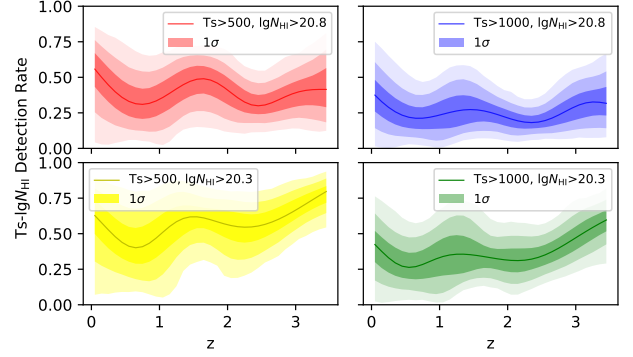


Figure 16. The detection rates and 3σ errors of 37 DLAs. The left panels are for $T_S > 500$ K and the right are for $T_S > 1000$ K. The upper panels are for $\lg N_{\text{HI}} \geq 20.8$ and the lower are for $\lg N_{\text{HI}} \geq 20.3$. The solid lines are the 3-Gauss fitting of KDEs, and the colored areas present their 3σ errors individually. Only the darkest 1σ regions are labeled in the legends.

Table 5. Multi-Gaussian fitting¹ of 0.2-bandwidth detection KDE curves

component	a	μ	σ
20.8-1000-1	0.4686 ± 0.1408	3.8692 ± 0.1728	0.4394 ± 0.0960
20.8-1000-2	0.7740 ± 0.0154	2.4748 ± 0.0154	0.8251 ± 0.0534
20.8-1000-3	0.7309 ± 0.0174	0.5183 ± 0.0324	0.7968 ± 0.0282
20.3-1000-1	0.5850 ± 0.0084	3.6992 ± 0.1645	1.6574 ± 0.2301
20.3-1000-2	0.2529 ± 0.0285	2.3546 ± 0.0097	0.4074 ± 0.0180
20.3-1000-3	0.5783 ± 0.0499	0.6383 ± 0.0187	0.6637 ± 0.0254
20.8-500-1	0.1109 ± 0.0156	2.4000 ± 0.0280	0.5282 ± 0.0506
20.8-500-2	0.1890 ± 0.0304	0.4603 ± 0.0331	0.3654 ± 0.0380
20.8-500-3	0.6210 ± 0.0126	1.5104 ± 0.1410	2.0000 ± 0.1354
20.3-500-1	0.2378 ± 1.1207	0.0602 ± 3.4411	0.5034 ± 2.3483
20.3-500-2	0.4541 ± 0.0020	2.2745 ± 0.0136	0.9268 ± 0.0163
20.3-500-3	0.3842 ± 2.2242	0.6983 ± 0.7163	0.4088 ± 0.2259

¹ The actual curve of detection rate is the result that one subtracts the 3-Gaussian fitting.

of 0 to 0.352 (1050-1450MHz). ASKAP covers 33000deg^2 (Allison et al. 2022) and the redshift of 0.4 to 1.0 (711.5-999.5MHz). As for the most remarkable instrument, the SKA1-Mid (SKA1M) covers about 30000deg^2 (KloECKNER et al. 2015; Weltman et al. 2020) and the redshift of 0 to 1. We list the predicted detection yield in Table 6 for each instrument and lower limit condition, and the 1σ errors are multiplicative result from the three-component bootstraps.

4 DISCUSSION

We emphasise that the S-L signal is a direct measurement, and its theoretical derivation is independent of Einstein's equation and Copernican principle (Yu et al. 2014), compared with other common cosmological probes like SNe Ia. But the different matter structures of every sightline in the signal propagation necessitates further studies of the inhomogeneity influence on the S-L signal.

The systematics of the S-L effect mainly contains two parts. First, the proper acceleration of the observer involves the earthly, solar, galactic and cosmological frames. The former two terms can be calculated in the highest level of cm/s (one-decade accumulation of S-L

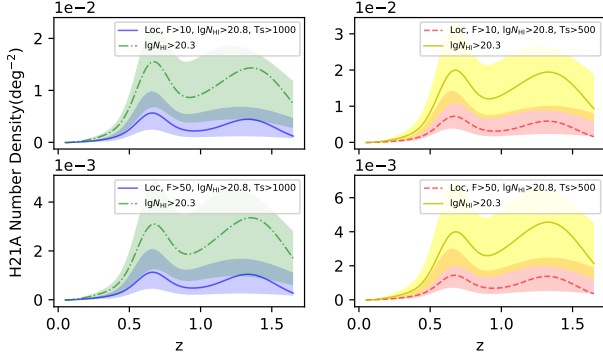


Figure 17. The potential H21A number density. The left panels are for $T_S > 1000\text{K}$ and the right are for $T_S > 500\text{K}$. The upper panels are for $F_{1.4\text{GHz}} > 10\text{mJy}$ and the lower are for $F_{1.4\text{GHz}} > 50\text{mJy}$. The lines and corresponding color areas are their density curves and 1σ errors.

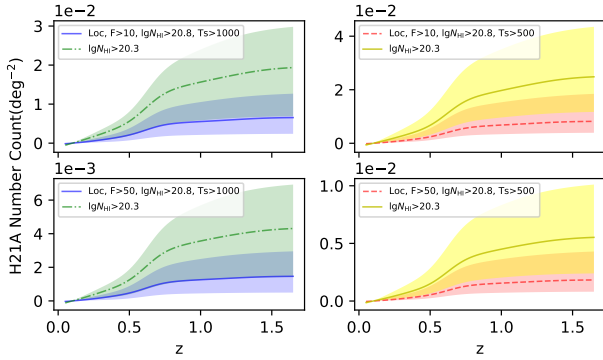


Figure 18. The potential H21A number count. The left panels are for $T_S > 1000\text{K}$ and the right are for $T_S > 500\text{K}$. The upper panels are for $F_{1.4\text{GHz}} > 10\text{mJy}$ and the lower are for $F_{1.4\text{GHz}} > 50\text{mJy}$. The lines and corresponding color areas are their count curves and 1σ errors.

signal) (Wright & Eastman 2014). The solar revolution around the galactic center can be accurately measured by pulsar timing (Zakamska & Tremaine 2005), Gaia Data Release 3 (Gaia Collaboration 2021) and VLBI (Xu et al. 2012; Titov & Krásná 2018) in mm/s/yr level which is the same as S-L signal. And the proper motion of extragalaxies is accessible by VLBI (Titov et al. 2011, 2022). The possible redshift uncertainties were given in Bolejko et al. (2019) and reviewed in Lu et al. (2022). Second, the peculiar motion of absorption line systems would impact the S-L signal. Combining the various physical conditions of DLAs (Dutta et al. 2017), the Neutral Mass (NM) ratio (Cold NM:Unstable NM:Warm NM = 28:20:52) in our galaxy (Murray et al. 2018), and Figure 14 from Kanekar et al. (2014), there do exist some DLAs with sharp absorptions as ideal targets for probing S-L signal. Additionally, the data process introduces new uncertainty when signal extraction and flux calibration. It is not the primary challenge but needs to maintain the same procedure and reform with new techniques.

Though simple statistical models like exponential can determine the number densities, and KDE would decrease generalization ability. We still use KDE for some reasons, most importantly to keep the method consistent in the data process. Second, as a non-parametric estimation, KDE needs less prior knowledge about the realistic dis-

Table 6. The detection yield of potential H21As in each condition

Telescope	$F_{\text{min}}/\text{mJy}$	$\lg(N_{\text{HI,min}}/\text{cm}^{-2})$	$T_{\text{S,min}}/\text{K}$	Prediction
FAST	>50	>20.8	>1000	$5.8^{+5.2}_{-4.2}$
			>500	$6.6^{+9.4}_{-4.0}$
		>20.3	>1000	$16.0^{+8.3}_{-11.4}$
	>10	>20.8	>1000	$18.7^{+17.8}_{-9.8}$
			>500	$26.2^{+21.4}_{-18.6}$
		>20.3	>1000	$30.0^{+39.4}_{-17.2}$
ASKAP	>50	>20.8	>1000	$72.1^{+33.3}_{-49.7}$
			>500	$84.7^{+73.2}_{-46.0}$
		>20.3	>1000	$31.5^{+32.2}_{-19.6}$
	>10	>20.8	>1000	$39.8^{+52.7}_{-20.8}$
			>500	$90.7^{+56.1}_{-57.8}$
		>20.3	>1000	$116.5^{+96.6}_{-63.0}$
SKA1M	>50	>20.8	>1000	$137.2^{+129.8}_{-81.1}$
			>500	$172.8^{+214.7}_{-83.6}$
		>20.3	>1000	$394.2^{+220.6}_{-250.1}$
	>10	>20.8	>1000	$506.7^{+385.6}_{-255.3}$
			>500	$37.8^{+37.1}_{-24.8}$
		>20.3	>1000	$46.6^{+62.3}_{-25.1}$
SKA1M	>50	>20.8	>1000	$107.0^{+63.7}_{-69.9}$
			>500	$135.0^{+114.7}_{-73.9}$
		>20.3	>1000	$165.8^{+150.2}_{-102.5}$
	>10	>20.8	>1000	$204.2^{+255.3}_{-102.7}$
			>500	$469.2^{+250.4}_{-293.8}$
		>20.3	>1000	$591.7^{+461.7}_{-302.9}$

tribution. Third, these simple-peak models are inadequate for multi-peak distribution. Fourth, when filtering data with different lower limits, some samples are discarded but close to the limits. However, KDE will record the contributions of these border-near samples. Although KDE is a sensitive method suffering more fluctuations from many factors, it provides similar features (a big bulge containing two peaks and a small bulge/peak) in the two panels of Figure 10, proving its robustness sufficiently.

The multi-Gaussian fittings for 2 components of KDEs in Table 3 and 5 offer poor constraints, but the fittings quite approach the KDEs and such a defect does not hinder our estimation.

Most used radio samples are radio-loud AGNs, but other information such as morphological and spectral types was not recorded. One can better grip their redshift distribution and radio luminosity function by dividing samples into more sub-types if acquiring more data, but now they are beyond our present reach.

With different radio datasets, it is necessary to compare their observations. The radio sources in CENSORS and Hercules were preliminarily selected by pioneering radio mapping and then probed by subsequent optical spectra. Original CENSORS (Brookes et al. 2008) optically observed 143 in all 150 sources, providing a 71% spectroscopic completeness. As for the rest, the $K-z$ (and $I-z$ for one source) relation was used to estimate their redshifts. Original Hercules (Waddington et al. 2001) with 72 sources, offered 47 spectroscopic redshifts, found 10 upper limits of redshift from literature, and estimated the broad-band photometric redshifts for the rest. Rigby et al. (2011) rearranged the two sets with some published reassessments. They selected a 135-sample subset for CENSORS with 73% spectroscopic completeness, and a 64-sample subset for Hercules with 40 spectroscopic and 20 photometric redshifts. As for CoNFIG-4 samples (Gendre & Wall 2009; Gendre et al. 2010), they

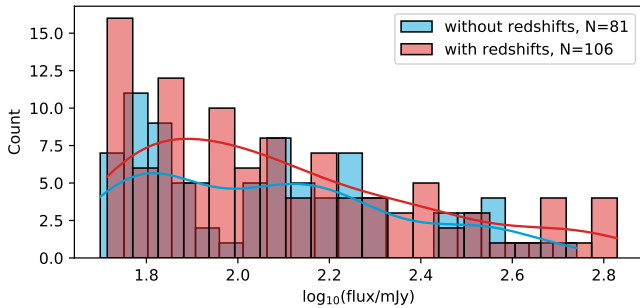


Figure 19. The histogram of CoNFIG-4 data for $F_{1.4\text{GHz}}$. The blue bars are for the samples without redshifts, and the blue line is their KDE curve, while the red ones are for those redshift "owners".

were selected from NVSS and FIRST (White et al. 1997) counterplots with complete Fanaroff–Riley morphology, and reviewed for their optical information. No observation was performed in CoNFIG papers, hence their redshift information was all from literature. For the samples without redshifts in CoNFIG-4, they have roughly similar but lower flux distribution compared to redshift "owners" in Figure 19, so it is hard to regard them as statistically less luminous in $F_{1.4\text{GHz}}$. But we find that most samples without redshifts do not have SDSS magnitudes recorded in the original data.

Optical selections inserted in observation unavoidably bias radio number density, but more datasets can provide a more robust prediction than a single one. Like the radio source number density per square degree sky (σ) at the end of section 3.1.3, only with three datasets, our estimated $\sigma_{50}=3.714$ can approach the NVSS value $\sigma_{50}=3.71$, while any single set corresponds a greater deviation.

Rao et al. (2017) provided abundant DLAs at low-redshift ($z \leq 1.65$) where the ground-based optical telescope can not directly observe. A reasonable speculation is that their preselection is biased by luminosity and dust extinction, having the risk of omitting some MgII absorbers, DLAs without MgII absorption, and deriving biasedly higher Ω_{DLA} . However, they found (in sec 4 of that article) no evidence for these effects at $z < 1.65$. And Kanekar's conclusion (Kanekar et al. 2014) also disapproves of this selection effect in the aspect of T_S distributions.

We notice that Dutta et al. (2017); Dutta (2019) advanced an absorption-blind or galaxy-selected approach, selecting a galaxy visually close to a background quasar (Quasar-Galaxy Pair, QGP) without the prior of any absorption toward the quasar. Their method is not intuitively biased as MgII preselection. We hope their project finds more QGPs for the distribution of radio DLASs.

In addition to Rao's and Neeleman's I-type DLAs, there exist other DLA datasets, e.g. Curran et al. (2016); Curran (2021). Curran's data provide 85 A-type and 56 I-type DLAs with $z > 0.1$. Although Curran's data cover wider redshift and more samples, they are collected from different observations. The decisive reason for discarding Curran's data is they do not contain N_{HI} which is included in Rao's data, and we want to use 2-dimension (z and N_{HI}) KDE for more features. Moreover, we plot Curran's and Rao's data in Figure 20, and Rao's KDE profile of I-type DLAs almost envelopes Curran's, exceptionally raising a bulge mainly because of the subset T15 (Turnshek et al. 2015) with z from 0.4 to 1.0. Besides, it is normal that total Curran's KDE profile covers Rao's, because the former contains extra A-type DLAs which are not suitable for S-L signal. Because over half DLAs (28 in 41) overlap Rao's samples, we do not plot Neeleman's KDE.

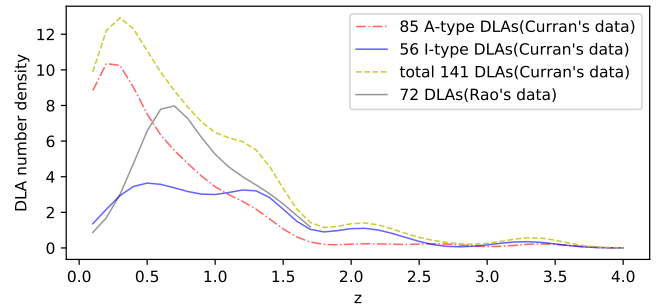


Figure 20. The KDE fittings (bandwidth=0.2) of two DLA datasets. The gray and yellow dashed curves are for the total two sets. The red dashed-dotted and blue curves are the A- and I-type DLAs in Curran's data separately.

The different tendencies in the low- z region between our KDE-derived and Rao's DLA number density in the left panel of Figure 13, apart from their wide z -bin, are mainly caused by Rao's modified DLA number density values at $z=0$ (Zwaan et al. 2005; Braun 2012). The modification is reasonable if we consider the left end of Curran's I-type KDE, which is slightly higher than Rao's in Figure 20, indicating the low- z shortage of Rao's samples. But the single value point $n_{\text{DLA}}(z=0)$ can not change the KDE result unless we have real low redshift DLAs to feed the algorithm.

Our $N_{\text{HI}}-T_S$ constraints for DLAs and the H21A-to-DLA proportional constant η , mainly rely on the 37-DLA data from Kanekar et al. (2014). Hence our results are inevitably affected by small samples and Poisson errors, and need more "full" information (z , N_{HI} , T_S and C_f) DLAs to overcome.

The recent study of DLAs detection yield includes the remarkable work from Allison et al. (2022), where they defined a completeness function \mathcal{C} with the 1000 mock spectra recovered from FLASH early survey of the GAMA 23 field (Allison et al. 2020), and used a N_{HI} frequency distribution function \mathcal{F} linearly interpolated from $z=0$ (Zwaan et al. 2005) and $z > 2$ (Bird et al. 2017), to predict the number of I-type and A-type DLAs in the ASKAP range. Future researchers will be enlightened to improve their N_{HI} frequency distribution. And their completeness function reminds us that more factors, such as signal-to-noise rate and blind-survey resolution (related to H21A's line width distribution), can be considered in prediction. These observational limitations from specific facilities are more concrete, and entail our further efforts.

An interesting difference between our prediction and the Allison's of ASKAP is, in our 37 DLAs, the low- N_{HI} I-type ones are more than the high- N_{HI} . Namely, our higher sensitivity condition in N_{HI} (to discover more DLAs) is to lower N_{HI} , while they need to increase it. Their complicated functions \mathcal{C} and \mathcal{F} , both relate to N_{HI} , and both are not plotted with respect to N_{HI} . Thus it is hard to say which one (\mathcal{C} or \mathcal{F}) dominates this difference.

Given more physical constraints to potential intervening H21As for FAST, our most optimistic expectation is quite small (80), around 1 or 2 order magnitude smaller than some previous work, such as 1500 (Zhang et al. 2021) from a local luminosity function estimation and 2600 (Jiao et al. 2020) for a decade CRAFTS observation (Zhang et al. 2019) with a simpler integration of eq. 8. However, our optimistic result approaches the magnitude of 100 from ALFALFA-survey estimation (Wu et al. 2015). Additionally, Zhang's 1500 result may omit that only about 10% AGNs are radio-loud and ignored AGN's z distribution.

5 CONCLUSION

In this paper, we make a small but important distinction between the global and dynamical \dot{a} and the local and observed \dot{v}_S at first, and emphasise that only the \dot{a} can express an actual expansion state for the whole Universe at one certain time, but it has not been measured model-independently.

Subsequently, in the bulk of the paper, we separately explore (i) n_R , the radio-source redshift number density per square degree via three datasets (with z and $F_{1.4\text{GHz}}$), (ii) n_D , the DLA redshift number density in the sightline through 87 DLAs from two low-redshift ($z \lesssim 1.65$) datasets (with z , N_{HI}), and (iii) κ , the DLA detection rate at given $N_{\text{HI}}-T_S$ limitations from an extra 37-DLA dataset and η (the fraction of H21As in DLAs). (1) Introducing the KDE method, we replace the traditional description of the n_R and n_D , and propose a data-based κ function, with multi-Gaussian profiles (Table 3, 4 and 5) of KDE curves. (2) Adopting the bootstrap method, we give the former three functions 1σ errors (Figure 10, 13 and 16). (3) We predict the potential blind-survey detection amounts (Table 6) for H21As with various limitations. At most optimistic conditions, FAST covers 80 H21As, ASKAP covers 500, and SKA1-Mid covers 600. Although our results are predicted H21A amount, it is convenient to turn them into DLA amount by dividing the proportional constant $\eta=0.62$.

The lack of BRS and DLA samples with "full" information is one of the crucial obstructions to our study. Nevertheless, with more potential H21As discovered in the future, it is a good chance to research H21As' physical essences and environments, as well as to revise the BRSs from a new aspect. And all this progress can propel our knowledge of the Universe, and help us to comprehend its expansion history and the underlying drivers.

ACKNOWLEDGEMENTS

We thank the anonymous referee for the kind comments that help us greatly to improve this paper. We acknowledge support from National SKA Program of China (2022SKA0110202) and National Natural Science Foundation of China (grants No. 61802428, 11929301).

DATA AVAILABILITY

The data we used in this paper are all open on the Internet. Three radio datasets (Rigby et al. 2011; Gendre et al. 2010) and three DLA datasets (Rao et al. 2006; Turnshek et al. 2015; Rao et al. 2017) are available in VizieR. The rest DLAs from Neeleman et al. (2016); Kanekar et al. (2014); Curran et al. (2016); Curran (2021) are directly extracted from their articles.

REFERENCES

Abazajian K. N., et al., 2009, *ApJS*, **182**, 543
 Alam S., et al., 2015, *ApJS*, **219**, 12
 Allison J. R., 2021, *MNRAS*, **503**, 985
 Allison J. R., et al., 2020, *MNRAS*, **494**, 3627
 Allison J. R., et al., 2022, *Publ. Astron. Soc. Australia*, **39**, e010
 Bird S., Garnett R., Ho S., 2017, *MNRAS*, **466**, 2111
 Bolejko K., Wang C., Lewis G. F., 2019, arXiv e-prints, p. arXiv:1907.04495
 Braun R., 2012, *ApJ*, **749**, 87
 Brookes M. H., Best P. N., Peacock J. A., Röttgering H. J. A., Dunlop J. S., 2008, *MNRAS*, **385**, 1297

Buchert T., van Elst H., Heinesen A., 2022, arXiv e-prints, p. arXiv:2202.10798
 Chakrabarti S., et al., 2022, arXiv e-prints, p. arXiv:2203.05924
 Codur R., Marinoni C., 2021, *Phys. Rev. D*, **104**, 123531
 Condon J. J., Cotton W. D., Greisen E. W., Yin Q. F., Perley R. A., Taylor G. B., Broderick J. J., 1998, *AJ*, **115**, 1693
 Cooke R., 2020, *MNRAS*, **492**, 2044
 Curran S. J., 2017a, *MNRAS*, **470**, 3159
 Curran S. J., 2017b, *A&A*, **606**, A56
 Curran S. J., 2021, *MNRAS*, **506**, 1548
 Curran S. J., Duchesne S. W., Divoli A., Allison J. R., 2016, *MNRAS*, **462**, 4197
 Darling J., 2012, *ApJ*, **761**, L26
 Davis T. M., Lineweaver C. H., 2001, in Durrer R., Garcia-Bellido J., Shaposhnikov M., eds, *American Institute of Physics Conference Series Vol. 555, Cosmology and Particle Physics*. pp 348–351 (arXiv:astro-ph/0011070), doi:10.1063/1.1363540
 Dong C., Gonzalez A., Eikenberry S., Jeram S., Likamonsavad M., Liske J., Stelter D., Townsend A., 2022, *MNRAS*, **514**, 5493
 Dutta R., 2019, *Journal of Astrophysics and Astronomy*, **40**, 41
 Dutta R., Srianand R., Gupta N., Momjian E., Noterdaeme P., Petitjean P., Rahmani H., 2017, *MNRAS*, **465**, 588
 Eikenberry S., et al., 2019, in *Bulletin of the American Astronomical Society*. p. 137 (arXiv:1907.08271)
 Esteves J., Martins C. J. A. P., Pereira B. G., Alves C. S., 2021, *MNRAS*, **508**, L53
 Gaia Collaboration 2021, *A&A*, **649**, A9
 Garon A. F., et al., 2019, *AJ*, **157**, 126
 Gendre M. A., Wall J. V., 2009, *MNRAS*, **394**, 1712
 Gendre M. A., Best P. N., Wall J. V., 2010, *MNRAS*, **404**, 1719
 Geréb K., Maccagni F. M., Morganti R., Oosterloo T. A., 2015, *A&A*, **575**, A44
 Grasha K., Darling J., Leroy A. K., Bolatto A. D., 2020, *MNRAS*, **498**, 883
 Gupta N., et al., 2016, in *MeerKAT Science: On the Pathway to the SKA*. p. 14 (arXiv:1708.07371)
 Gupta N., et al., 2021, *ApJ*, **907**, 11
 Heinesen A., Macpherson H. J., 2022, *J. Cosmology Astropart. Phys.*, **2022**, 057
 Jiao K., Zhang J.-C., Zhang T.-J., Yu H.-R., Zhu M., Li D., 2020, *J. Cosmology Astropart. Phys.*, **2020**, 054
 Kanekar N., et al., 2014, *MNRAS*, **438**, 2131
 Kloeckner H. R., et al., 2015, in *Advancing Astrophysics with the Square Kilometre Array (AASKA14)*. p. 27 (arXiv:1501.03822)
 Koribalski B. S., et al., 2020, *Ap&SS*, **365**, 118
 Li D., et al., 2018, *IEEE Microwave Magazine*, **19**, 112
 Liske J., et al., 2008, *MNRAS*, **386**, 1192
 Loeb A., 1998, *ApJ*, **499**, L111
 Lu C.-Z., Jiao K., Zhang T., Zhang T.-J., Zhu M., 2022, *Physics of the Dark Universe*, **37**, 101088
 Ma Z., et al., 2019, *ApJS*, **240**, 34
 Marcos-Caballero A., Vielva P., Martinez-Gonzalez E., Finelli F., Gruppiso A., Schiavon F., 2013, arXiv e-prints, p. arXiv:1312.0530
 Matthews A. M., Condon J. J., Cotton W. D., Mauch T., 2021, *ApJ*, **909**, 193
 Melia F., 2022, *European Journal of Physics*, **43**, 035601
 Mishra P., 2022, *Phys. Rev. D*, **105**, 063520
 Moresco M., et al., 2022, arXiv e-prints, p. arXiv:2201.07241
 Murray C. E., Stanimirović S., Goss W. M., Heiles C., Dickey J. M., Babler B., Kim C.-G., 2018, *ApJS*, **238**, 14
 Neeleman M., Prochaska J. X., Ribaud J., Lehner N., Howk J. C., Rafelski M., Kanekar N., 2016, *ApJ*, **818**, 113
 Noterdaeme P., et al., 2012, *A&A*, **547**, L1
 Planck Collaboration 2020, *A&A*, **641**, A6
 Prochaska J. X., Wolfe A. M., 2009, *ApJ*, **696**, 1543
 Rao S. M., Turnshek D. A., Nestor D. B., 2006, *ApJ*, **636**, 610
 Rao S. M., Turnshek D. A., Sardane G. M., Monier E. M., 2017, *MNRAS*, **471**, 3428
 Rigby E. E., Best P. N., Brookes M. H., Peacock J. A., Dunlop J. S., Röttgering H. J. A., Wall J. V., Ker L., 2011, *MNRAS*, **416**, 1900

- Sadler E. M., et al., 2020, *MNRAS*, **499**, 4293
- Sandage A., 1962, *ApJ*, **136**, 319
- Schmidt S. J., Connolly A. J., Hopkins A. M., 2006, *ApJ*, **649**, 63
- Titov O., Krásná H., 2018, *A&A*, **610**, A36
- Titov O., Lambert S. B., Gontier A. M., 2011, *A&A*, **529**, A91
- Titov O., et al., 2022, *MNRAS*, **512**, 874
- Toba Y., et al., 2019, *ApJS*, **243**, 15
- Turnshek D. A., Monier E. M., Rao S. M., Hamilton T. S., Sardane G. M., Held R., 2015, *MNRAS*, **449**, 1536
- Waddington I., Dunlop J. S., Peacock J. A., Windhorst R. A., 2001, *MNRAS*, **328**, 882
- Weltman A., et al., 2020, *Publ. Astron. Soc. Australia*, **37**, e002
- White R. L., Becker R. H., Helfand D. J., Gregg M. D., 1997, *ApJ*, **475**, 479
- Wright J. T., Eastman J. D., 2014, *PASP*, **126**, 838
- Wu Z. Z., Haynes M. P., Giovanelli R., Zhu M., Chen R. R., 2015, *Acta Astronomica Sinica*, **56**, 112
- Xu J., Han J. L., 2014, *MNRAS*, **442**, 3329
- Xu M. H., Wang G. L., Zhao M., 2012, *A&A*, **544**, A135
- Yu H.-R., Zhang T.-J., Pen U.-L., 2014, *Phys. Rev. Lett.*, **113**, 041303
- Yu H.-R., Pen U.-L., Zhang T.-J., Li D., Chen X., 2017, *RAA*, **17**, 049
- Zakamska N. L., Tremaine S., 2005, *AJ*, **130**, 1939
- Zhang K., et al., 2019, *Science China Physics, Mechanics, and Astronomy*, **62**, 959506
- Zhang B., Zhu M., Wu Z.-Z., Yu Q.-Z., Jiang P., Yue Y.-L., Huang M.-L., Hao Q.-L., 2021, *MNRAS*, **503**, 5385
- Zwaan M. A., van der Hulst J. M., Briggs F. H., Verheijen M. A. W., Ryan-Weber E. V., 2005, *MNRAS*, **364**, 1467
- de Zotti G., Massardi M., Negrello M., Wall J., 2010, *A&ARv*, **18**, 1

This paper has been typeset from a $\text{\TeX}/\text{\LaTeX}$ file prepared by the author.